



In situ embedding Co₉S₈ into nitrogen and sulfur codoped hollow porous carbon as a bifunctional electrocatalyst for oxygen reduction and hydrogen evolution reactions

Shaolong Zhang^{a,b,c}, Dong Zhai^{d,e}, Tingting Sun^b, Aijuan Han^b, Yanliang Zhai^f,
Weng-Chon Cheong^b, Yi Liu^d, Chenliang Su^a, Dingsheng Wang^{b,*}, Yadong Li^b

^a SZU-NUS Collaborative Innovation Center for Optoelectronic Science & Technology, International Collaborative Laboratory of 2D Materials for Optoelectronics Science and Technology of Ministry of Education, College of Physics and Optoelectronic Engineering, Shenzhen University, Shenzhen 518060, China

^b Department of Chemistry, Tsinghua University, Beijing 100084, China

^c Guangdong Provincial Key Laboratory of Nano-Micro Materials Research, Peking University Shenzhen Graduate School, Shenzhen 518055, China

^d Materials Genome Institute and International Centre for Quantum and Molecular Structures, Department of Physics, Shanghai University, Shanghai 200444, China

^e Institute of Molecular Sciences and Engineering, Shandong University, Qingdao 266237, China

^f State Key Laboratory of Heavy Oil Processing and the Key Laboratory of Catalysis of CNPC, China University of Petroleum, Beijing 102249, China

ARTICLE INFO

Keywords:

Cobalt sulfide
Nitrogen and sulfur codoped hollow porous carbon
Electrocatalysts
Oxygen reduction reaction
Hydrogen evolution reaction

ABSTRACT

The oxygen reduction reaction (ORR) and hydrogen evolution reaction (HER) are critical processes for many energy conversion technologies, where efficient catalyst plays a key role in these reactions. Here we report a novel *in situ* strategy to embed Co₉S₈ nanoparticles (NPs) into nitrogen and sulfur codoped hollow porous carbon (Co₉S₈@N-S-HPC). In this strategy, the ZIF-8 surface is firstly decorated by cobalt thiourea, and then coated with a shell of polymeric resorcinol-formaldehyde, followed by a high temperature pyrolysis treatment. The resulting Co₉S₈@N-S-HPC shows comparable catalytic activity for ORR compared with commercial 20 wt% Pt/C catalyst and superior long-term stability under alkaline conditions. Simultaneously, Co₉S₈@N-S-HPC also exhibits an excellent HER activity with low onset overpotential of 68 mV, a small Tafel slope of 78 mV per decade and a long-term durability in alkaline medium. First-principles calculations reveal that Co₉S₈ particle can anchor in N-S-HPC via a Co-S bond and enhance the binding of Co₉S₈ and N-S-HPC. The N-S-HPC can affect the electronic structure of supported Co₉S₈ strongly. The combined experimental and theoretical investigation show the outstanding ORR and HER performances of Co₉S₈@N-S-HPC are attributed to its unique nanostructure and synergistic interactions between Co₉S₈ NPs and N-S-HPC.

1. Introduction

Along with the declining of fossil fuel reserves and growing environmental pollution issues, increased incentive has been devoted to developing next generation power sources. Energy conversion and storage systems such as fuel cells, water electrolysis and metal–air batteries have been recognized as the environmentally benign solutions to deal with the issues. The oxygen reduction reaction (ORR) is a core process for these solutions [1–3]. Besides, the hydrogen evolution reaction (HER) in water-splitting devices could supply the clean energy carrier of hydrogen [4–6]. Both of the reactions are the cornerstone of many energy conversion and storage systems [7–9]. To date, the noble metal Pt and Pt-based materials are still the most active catalysts for the ORR and HER processes. Nevertheless, the prohibitive cost and natural

scarcity of these Pt-based catalysts with inferior durability at the cathode greatly limit their widespread use as the promising catalysts [10–13]. Hence, it remains highly challenging and great technological importance to obtain efficient and cost-effective bifunctional catalysts for ORR and HER.

To date, many efforts have been devoted to developing novel alternatives to Pt-based electrocatalysts. Recently, transition metal sulfides, particularly molybdenum sulfide, nickel sulfide and cobalt sulfide, have attracted great attention because of their earth abundance, low cost and excellent electronic properties. Among them, Co₉S₈ has been proposed as a potential material for high-performance electrocatalysts. According to the quantum chemistry calculations, the electrocatalytic behavior of Co₉S₈ is similar to that of Pt electrode [14]. However, the drawbacks of pristine Co₉S₈, such as intrinsic poor

* Corresponding author.

E-mail address: wangdingsheng@mail.tsinghua.edu.cn (D. Wang).

<https://doi.org/10.1016/j.apcatb.2019.04.096>

Received 20 November 2018; Received in revised form 27 April 2019; Accepted 29 April 2019

Available online 01 May 2019

0926-3373/© 2019 Elsevier B.V. All rights reserved.

electrical conductivity, instability and low surface area, still severely limit its practical applications [15]. In this regard, combining Co_9S_8 with porous and conductive carbonaceous materials would be a promising technology to enhance the electrocatalytic activity [16,17]. Specifically, the porous carbon doping with heteroatoms have exhibited outstanding electrochemical performances, due to their asymmetrical electron spin density, unique charge polarization and mitigatory volume variation [18–21]. In addition, hollow carbon nanostructures with hollow space and thin shells can endow the carbon materials with low density, high surface area and homogeneous reaction environment and so on. Such hollow structure would be desirable to provide improved conductivity, abundant active sites and accelerated mass transport [22–25]. More importantly, exploring an appropriate way for combining the Co_9S_8 with heteroatom-doped carbon is critical. An efficient protocol is developed for the *in situ* combination of Co_9S_8 and heteroatom-doped carbon into the hybrid architecture, which could provide synergistic advantages [26]. However, it is still a challenge to take both advantages of Co_9S_8 and heteroatom-doped carbon with hollow nanostructures to design a composite with excellent electrochemical performance.

Herein, we demonstrate a novel strategy for the *in situ* synthesis of Co_9S_8 embedded into nitrogen and sulfur codoped hollow porous carbon. The strategy involves decorating ZIF-8 with cobalt thiourea, coating the decorated ZIF-8 with a resorcinol-formaldehyde layer, and subsequent thermal pyrolysis at high temperature in argon flow. This method can guarantee the intimate contact of Co_9S_8 and N-S-HPC and provide synergistic advantages. In the as-prepared sample of $\text{Co}_9\text{S}_8@\text{N-S-HPC}$, the hollow porous carbon capsules are doped with N and S, and Co_9S_8 NPs are embedded into the carbon capsules. According to the combined experimental and theoretical study, the particular nanostructures and the synergistic effect of these active species, $\text{Co}_9\text{S}_8@\text{N-S-HPC}$ exhibits an excellent electrocatalytic performance toward ORR and HER in alkaline media.

2. Experimental section

2.1. Preparation of ZIF-8

The synthesis of ZIF-8 can be found in our previous report [27]. $\text{Zn}(\text{NO}_3)_2 \cdot 6\text{H}_2\text{O}$ was dissolved in a DMF-MeOH-EtOH ($v/v/v = 3:1:1$). 2-methylimidazole was dissolved in DMF-MeOH ($v/v = 4:1$). Then, both solutions were mixed together, and stirred for 24 h at room temperature. The product was collected by centrifugation, washed and dried under vacuum at 100 °C for further use.

2.2. Preparation of $\text{Co}(\text{TU})$ -ZIF-8

Firstly the cobalt thiourea complex ($\text{Co}(\text{TU})_4(\text{NO}_3)_2$) was prepared according to the reported method and named as $\text{Co}(\text{TU})$ [28]. Then ZIF-8 and $\text{Co}(\text{TU})$ in a mass ratio of 10:1.5 were dissolved in a hot acetone solution, and the solution was vigorously stirred until all the solvent evaporated. The product was finely ground and named as $\text{Co}(\text{TU})$ -ZIF-8.

2.3. Preparation of $\text{Co}(\text{TU})$ -ZIF-8@RF

The $\text{Co}(\text{TU})$ -ZIF-8@RF was prepared according to the previous reported method [29]. Briefly, a mixture of resorcinol (15 mg), formaldehyde solution (3 g) and cetyltrimethylammonium bromide (15 mg) in 60 ml of deionized water was stirred for 30 min. Then 200 mg of $\text{Co}(\text{TU})$ -ZIF-8 were dispersed and sonicated for 10 min and followed by stirring for 24 h at room temperature. The product was collected by centrifugation, washed with methanol and H_2O , and dried under a vacuum overnight. The product was named as $\text{Co}(\text{TU})$ -ZIF-8@RF.

2.4. Preparation of $\text{Co}_9\text{S}_8@\text{N-S-HPC}$

The as-prepared $\text{Co}(\text{TU})$ -ZIF-8@RF was transferred to a tube furnace and pyrolysis under atmosphere of argon at 900 °C for 120 min. And the heating rate was set at 5 °C min^{-1} . After that, the materials were cooled down to room temperature naturally. The final product is referred to as $\text{Co}_9\text{S}_8@\text{N-S-HPC}$. For comparison, the Co_9S_8 NPs were obtained by the hydrothermal method [30]. Preparation of N-S-HPC was similar to that of $\text{Co}_9\text{S}_8@\text{N-S-HPC}$ but starting from TU-ZIF-8.

2.5. Electrochemical measurements

Electrochemical measurements were performed by a CHI 760E electrochemical workstation (Shanghai Chenhua, China) with a three-electrode system. And a Ag/AgCl (saturated KCl) electrode was selected as the reference electrode, a graphite rod was used as the counter electrode and a glassy carbon (GC) round disk electrode (RDE) of 5 mm in diameter coated with the catalyst ink functioning as the working electrode. The working electrode was prepared as follows. Typically, 5 mg of catalyst was mixed with 980 μL ethanol and 20 μL 5% Nafion solution and sonicated for at least 30 min to form homogeneous catalyst inks. Then 10 μL of the as-prepared inks was dropped onto the GC surface and dried in air for further testing and the catalyst loading was $\sim 0.26 \text{ mg cm}^{-2}$. ORR measurements were conducted in O_2 -saturated 0.1 M KOH solution, and HER measurements were conducted in N_2 -purged 1 M KOH solution. All potentials were normalized to the reversible hydrogen electrode (RHE) using the Nernst equation: $E_{\text{RHE}} = E_{\text{Ag}/\text{AgCl}} + 0.059 \text{ pH} + E^0_{\text{Ag}/\text{AgCl}}$ ($E^0_{\text{Ag}/\text{AgCl}} = 0.197$).

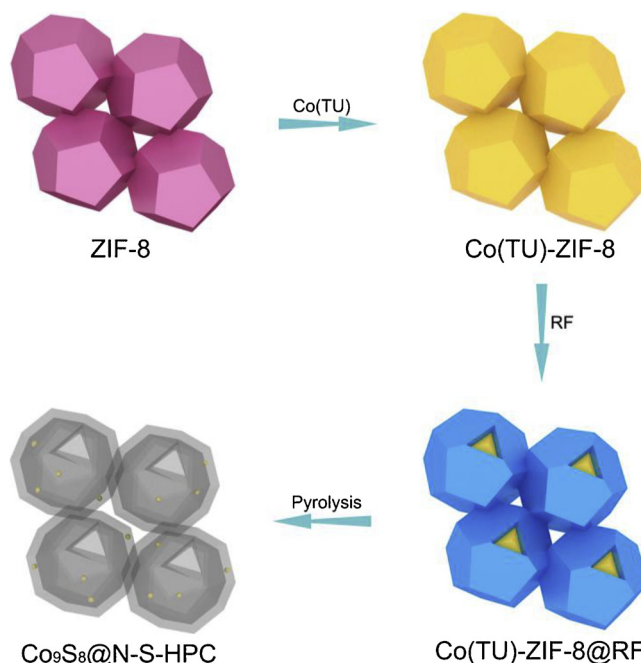
Other details can be found in Supporting information.

Material characterization and details of DFT calculations are described in Supporting information.

3. Results and discussion

3.1. Synthesis and characterization of $\text{Co}_9\text{S}_8@\text{N-S-HPC}$

The fabrication process included three steps (Scheme 1). Firstly, the synthesized ZIF-8 was immersed in a hot acetone solution containing cobalt thiourea ($\text{Co}(\text{TU})$) and stirred until all the solvent was



Scheme 1. Schematic illustration of the synthetic route of $\text{Co}_9\text{S}_8@\text{N-S-HPC}$.

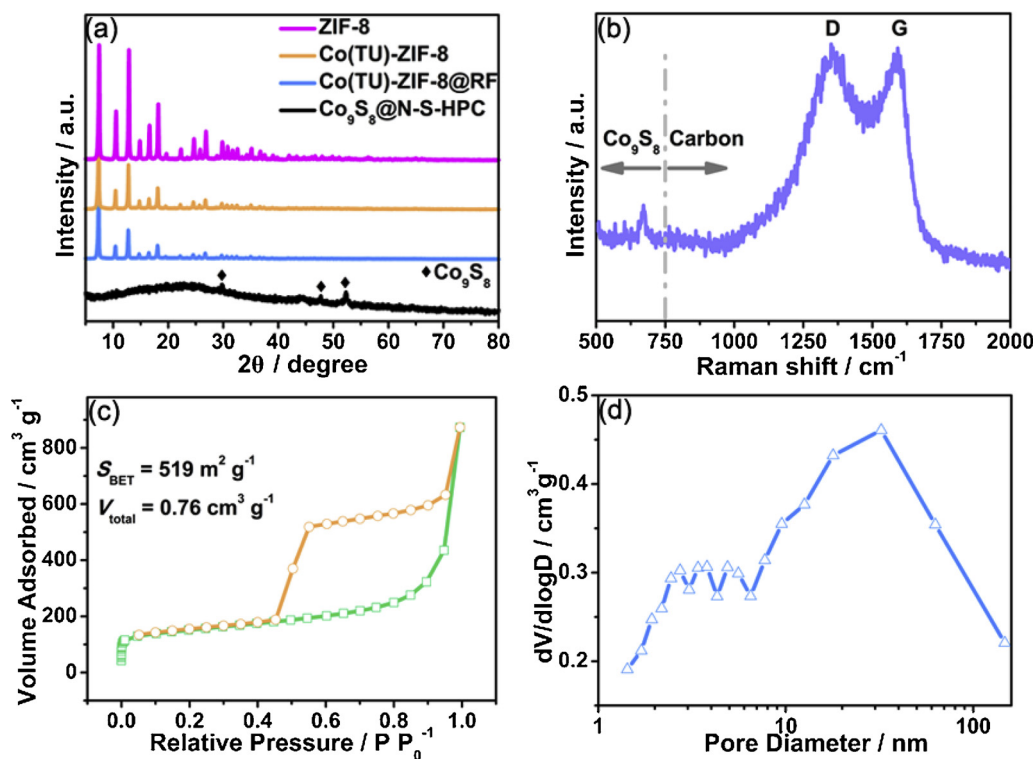


Fig. 1. (a) Powder XRD patterns of the samples, (b) Raman spectra of Co₉S₈@N-S-HPC, (c) Nitrogen adsorption/desorption curves of Co₉S₈@N-S-HPC and (d) Pore size distribution of Co₉S₈@N-S-HPC.

evaporated, yielding Co(TU)-ZIF-8. Since the pore apertures of ZIF-8 is around 0.34 nm, Co(TU) with bulky steric size can only be supported on the surface of ZIF-8 instead of the pore and matrices of ZIF-8 [31]. Secondly, the surface of Co(TU)-ZIF-8 was covered by a thin layer of resorcinol-formaldehyde (RF) (denoted as Co(TU)-ZIF-8@RF) by dispersing Co(TU)-ZIF-8 into a solution of resorcinol and formaldehyde. Lastly, Co(TU)-ZIF-8@RF was treated at 900 °C under a protective atmosphere of inert argon, and finally the Co₉S₈ embedded into nitrogen and sulfur codoped hollow porous carbon (Co₉S₈@N-S-HPC) was obtained.

Compared with the standard simulated XRD pattern from the published ZIF-8 structure data, the product of ZIF-8 could be assigned to SOD-type structures and pure-phase ZIF-8 material (Fig. 1a) [27]. The samples of Co(TU)-ZIF-8 and Co(TU)-ZIF-8@RF show similar XRD patterns to ZIF-8, indicating that both impregnation and coating processes have no significant effect on the crystal structure of ZIF-8. The XRD pattern of Co₉S₈@N-S-HPC shows a broad characteristic diffraction peak at ~24°, which is attributed to the (002) planes of the graphitic carbon. And the diffraction peaks that agreed well with the Co₉S₈ are also observed. The diffraction peaks located at around 29.6°, 47.6° and 52.1° correspond to the (311), (333) and (440) phase planes of typical crystalline Co₉S₈, respectively [32]. These phenomena demonstrate that Co(TU)-ZIF-8@RF transformed into carbonaceous materials and Co(TU) formed Co₉S₈ effectively during the pyrolysis process. Meanwhile, a set of weak Raman bands < 750 cm⁻¹ that perfectly indexed to Co₉S₈ are observed from Raman spectra of Co₉S₈@N-S-HPC (Fig. 1b) [30]. Two obvious peaks at around 1350 cm⁻¹ and 1590 cm⁻¹ are also observed, corresponding to the D-band and G-band of typical carbon-based materials [33]. The ratio of the relative intensity of the D-band to G-band (I_D/I_G) is 1.05, which means that the disordered carbon content is almost the same as that of graphitic carbon. On one hand, a large number of defects or disordered sites present in the carbon structure, ascribing to the N and S dopants in the carbon structure and the amorphous feature of carbon. The defects are favorable for increasing catalytically active sites and enhancing electrocatalytic performance.

On the other hand, the high pyrolysis temperature can increase graphitization degree of the carbon, which would benefit to the electronic conductivity and corrosion resistance during electrocatalysis [34]. Nitrogen sorption isotherm of Co₉S₈@N-S-HPC exhibits a type IV curve with a large hysteresis loop (Fig. 1c), revealing a large BET surface area of 519 m² g⁻¹ and pore volume of 0.76 cm³ g⁻¹. What's more, hierarchical pore can be clearly distinguished from the pore size distribution curve (Fig. 1d). The large surface area and hierarchical pore could be favorable for more exposed active sites and rapid mass transport, which should be considered for structural design of excellent electrocatalysts [35].

The scanning electron microscopy (SEM) images (Figs. 2a and S2) show that Co₉S₈@N-S-HPC consists of well-defined polyhedral morphology with edge lengths of about 100–300 nm. The morphology of the obtained product is similar to that of the parent ZIF-8 and the two intermediates (Fig. S3), indicating the retention of the conformal shape after pyrolysis treatment. And no obvious Co₉S₈ NPs are observed from the magnified SEM image. This discloses that Co₉S₈ NPs are not on the carbon surface. The broken polyhedral morphology is observed with an open gap and cavity (inset of Fig. 2a), showing the hollow nature of the products. The transmission electron microscopy (TEM) (Fig. 2b) image confirms the hollow capsules structure of Co₉S₈@N-S-HPC. The thickness of capsule wall is around 10–15 nm. The Co₉S₈ NPs are well embedded in walls of hollow carbon capsules with an average size of 8–10 nm. Also, no Co₉S₈ NPs can be observed on the exterior of the carbon shell, which agrees well with the SEM results. It is worth noting that, this is advantageous for preventing the dissolution and agglomeration of Co₉S₈ NPs, thus boosting the electrochemical activity and stability. High-resolution TEM (HRTEM) (Fig. S4) shows that the lattice spacing is ~0.29 nm, which is indexed to the (311) plane of cubic Co₉S₈ structure and in agreement with the X-ray diffraction results [36]. High-angle annular dark-field scanning transmission electron microscopy (HAADF-STEM) image (Fig. 2c) also demonstrates that the Co₉S₈ NPs are embedded in walls of hollow carbon capsules, an amount of around 1.1 wt% Co for Co₉S₈@N-S-HPC is also confirmed by ICP-OES result.

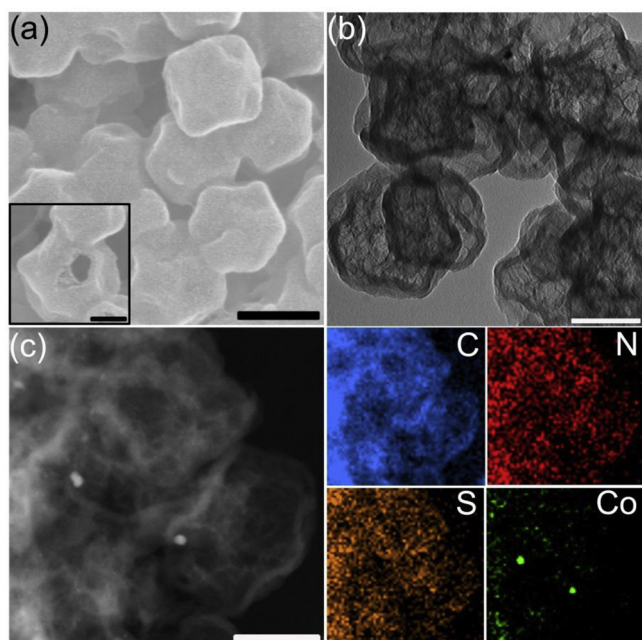


Fig. 2. (a) SEM images of $\text{Co}_9\text{S}_8/\text{N-S-HPC}$ (scale bars 250 nm), (b) TEM image of $\text{Co}_9\text{S}_8/\text{N-S-HPC}$ (scale bar 100 nm), (c) HAADF-STEM image of $\text{Co}_9\text{S}_8/\text{N-S-HPC}$, corresponding element maps showing the distribution of C (blue), N (red), S (yellow) and Co (green) (scale bar 100 nm). Inset in a): high-magnification SEM image, scale bar 100 nm. (For interpretation of the references to colour in this figure legend, the reader is referred to the web version of this article).

And the corresponding element maps confirm the coexisting of C, N, S, and Co elements. In addition, N is distributed almost entirely on the carbon surface, which indicates the incorporation of N in the carbon matrix. And S element exists not only on the Co_9S_8 NPs surface but also on the carbon surface, demonstrating the presence of sulfur with cobalt and sulfur doped in the carbon [37].

X-ray photoelectron spectroscopic (XPS) was performed to study the elemental composition and chemical status of $\text{Co}_9\text{S}_8/\text{N-S-HPC}$. The XPS survey reveals the co-existence of the C, O, N, S and Co elements (Fig. S5). The high resolution spectrum of C 1s can be divided into several peaks (Fig. 3a). The binding energies of 284.9 and 285.8 eV respectively correspond to C–S and C–N/O, demonstrating the co-doping of S and N into the carbon matrix [38,39]. The spectrum of N 1s is fitted to three peaks, assigned to the pyridinic N (398.7 eV), pyrrolic N (400.1 eV), and graphitic N (401.0 eV) (Fig. 3b). Obviously, pyridinic N and graphitic N are the dominant species, which are believed to be favorable for enhancing the ORR and HER activities [39,40]. In the high-resolution S 2p spectrum (Fig. 3c), the peaks at 163.9 eV and 165.0 eV are in agreement with S 2p_{3/2} and S 2p_{1/2} positions associated with C–S–C. Again, S doped into carbon skeletons is confirmed. Also, the binding energy at around 162.2 eV can be assigned to cobalt sulfide [32]. Furthermore, in the Co 2p region (Fig. 3d), the peaks at around 778.7 eV and 781.0 eV are assigned to the Co 2p_{3/2}, while the peaks at around 793.8 eV and 796.8 eV are ascribed to the Co 2p_{1/2}. These doublets are assigned to Co^{3+} and Co^{2+} , which are consistent with the literature and confirm the formation of Co_9S_8 [41–43].

3.2. Electrocatalytic performance

The ORR activities of the samples were studied in 0.1 M KOH solution. In our experiment, four different samples Co_9S_8 NPs, N-S-HPC, 20 wt% Pt/C and $\text{Co}_9\text{S}_8/\text{N-S-HPC}$ are selected for ORR comparison. Linear scanning voltammetry (LSV) plots indicate that the $\text{Co}_9\text{S}_8/\text{N-S-HPC}$ exhibits the best ORR catalytic performance, superior to the individual Co_9S_8 and N-S-HPC due to the synergetic effect between Co_9S_8

and N-S-HPC. And the activity of $\text{Co}_9\text{S}_8/\text{N-S-HPC}$ is even slightly better than that of the commercial 20 wt% Pt/C. The $\text{Co}_9\text{S}_8/\text{N-S-HPC}$ provides a highly positive ORR with an onset potential (E_{on}) of ~ 0.99 V vs. RHE and a half-wave potential ($E_{1/2}$) of ~ 0.85 V vs. RHE, which are comparable to those of Pt/C (~ 0.97 V and ~ 0.83 V vs. RHE, respectively) (Fig. 4a). The $E_{1/2}$ of $\text{Co}_9\text{S}_8/\text{N-S-HPC}$ is comparable to those obtained by others recently reported non-precious metal ORR electrocatalysts (Table S1), indicating an excellent ORR electrocatalytic activity of $\text{Co}_9\text{S}_8/\text{N-S-HPC}$ in alkaline media. Rotating disk electrode (RDE) tests were performed at different rotating speeds, the LSVs of $\text{Co}_9\text{S}_8/\text{N-S-HPC}$ show that the E_{on} is invariant for all rotating speeds, while the current density is enhanced with increasing rotating speed due to the improved mass transport at higher speeds. The Koutecky-Levich (K–L) equation was used to calculate the number of electrons transferred (n). The corresponding K–L plots (Fig. 4b) show excellent linearity and near coincidence, suggesting first-order reaction kinetics with respect to the concentration of dissolved O_2 and similar electron transfer numbers for ORR at different potentials. The n was obtained from the slope of the K–L plots and the n value is ~ 3.9 at 0.40–0.60 V, indicating a quasi-four electron transfer pathway where O_2 is reduced to H_2O [44]. This is similar to that of Pt/C, unlike two electron transfer pathway where O_2 is reduced to H_2O_2 , four electron transfer pathway is preferred in fuel cell processes [45,46]. The excellent ORR activity of $\text{Co}_9\text{S}_8/\text{N-S-HPC}$ is also verified by the Tafel slope, $\text{Co}_9\text{S}_8/\text{N-S-HPC}$ has a small Tafel slope (75 mV dec^{-1}) at low overpotentials, which is comparable to that of Pt/C (79 mV dec^{-1}) (Figure S6), indicating that $\text{Co}_9\text{S}_8/\text{N-S-HPC}$ has a desirable kinetic property. Because a lower value of the Tafel slope implies faster kinetics [47]. The long-term stability of $\text{Co}_9\text{S}_8/\text{N-S-HPC}$ was also investigated, $\text{Co}_9\text{S}_8/\text{N-S-HPC}$ retained similar LSV curves even after 5000 continuous cycles between 0.6 and 1.0 V at a sweep rate of 50 mV s^{-1} in O_2 -saturated 0.1 M KOH (Fig. 4c), demonstrating the outstanding catalytic durability of $\text{Co}_9\text{S}_8/\text{N-S-HPC}$. These results indicate that Co_9S_8 dispersed within nitrogen and sulfur codoped hollow porous carbon are efficient electrocatalysts for enhancing the ORR performance.

The HER activities of the samples were evaluated in 1 M KOH solution. Individual N-S-HPC and Co_9S_8 display negligible and poor HER performance. 20 wt% Pt/C shows excellent HER activity with a near-zero onset overpotential as expected. Impressively, the $\text{Co}_9\text{S}_8/\text{N-S-HPC}$ shows a low onset overpotential of ~ 68 mV. What's more, to achieve the current density of 10 mA cm^{-2} , $\text{Co}_9\text{S}_8/\text{N-S-HPC}$ only requires an overpotential of ~ 173 mV (Fig. 4d). Strikingly, this low overpotential indicates that $\text{Co}_9\text{S}_8/\text{N-S-HPC}$ is one of the best HER electrocatalysts in basic solution, and the overpotential of ~ 173 mV is comparable to or smaller than that of representative noble-metal-free electrocatalysts (Table S2). To gain insights into the advantage of the catalytic activity of $\text{Co}_9\text{S}_8/\text{N-S-HPC}$ for HER, electrochemical impedance spectroscopy (EIS) analysis at the selected overpotential of 100 mV was performed. An equivalent circuit according to the simple Randles cell model was used to fit the EIS Nyquist plots. The charge transfer controls the kinetics at the electrode interface is suggested by observed one semicircle in the Nyquist plot, and the diameter of the semicircle reflects the charge-transfer resistance (R_{ct}). It can be seen that the R_{ct} value for $\text{Co}_9\text{S}_8/\text{N-S-HPC}$ is only 28Ω (Fig. S7), suggesting the fast charge transport efficiency of $\text{Co}_9\text{S}_8/\text{N-S-HPC}$. For further insight into HER mechanism, reaction kinetics were evaluated from the Tafel plots, which are determined from the equation of $\eta = b \log(j) + a$ (where j is the current density and b is the Tafel slope). The Pt/C exhibits a Tafel slope of 36 mV dec^{-1} , and the Tafel slope for $\text{Co}_9\text{S}_8/\text{N-S-HPC}$ is 78 mV dec^{-1} , which is lower than that of individual Co_9S_8 (163 mV dec^{-1}) and N-S-HPC (176 mV dec^{-1}) (Fig. 4e). The present Tafel slope is also substantially lower or comparable to those obtained in other reported HER catalysts [48–50]. It can be concluded that the synergistic effects between Co_9S_8 and N-S-HPC are a significant role to improve the catalytic activity. Besides, the value of Tafel slope of $\text{Co}_9\text{S}_8/\text{N-S-HPC}$ indicates that the HER mechanism follows the Volmer-Heyrovsky

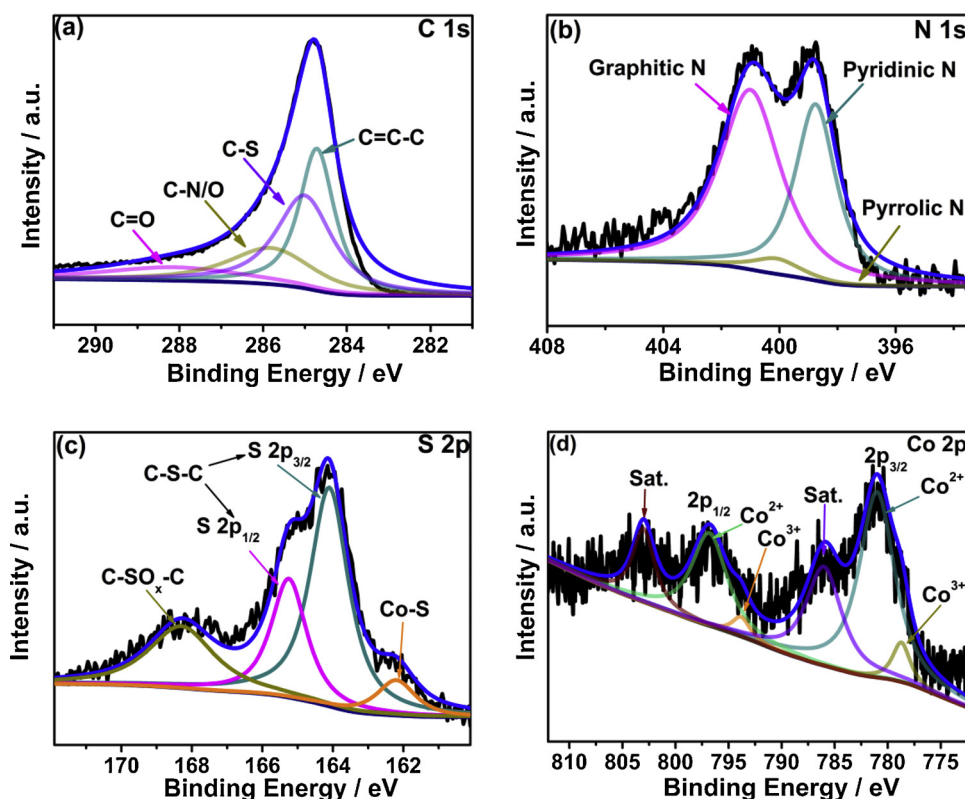


Fig. 3. High-resolution (a) C1s, (b) N 1s, (c) S 2p and (d) Co 2p XPS spectra of $\text{Co}_9\text{S}_8@\text{N-S-HPC}$.

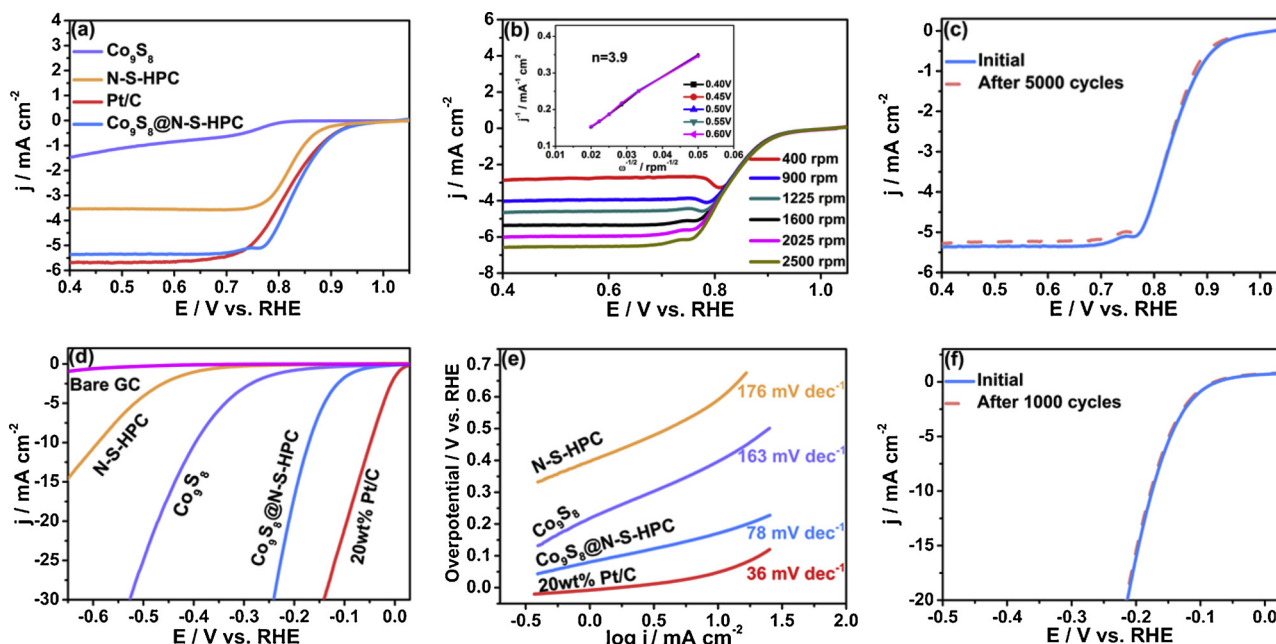


Fig. 4. (a) LSV curves of samples for the ORR at 10 mV s^{-1} and a rotating speed of 1600 rpm, (b) LSV curves of $\text{Co}_9\text{S}_8@\text{N-S-HPC}$ at various rotating speeds (inset: K-L plots of $\text{Co}_9\text{S}_8@\text{N-S-HPC}$ at various potentials and electron transfer number), (c) LSV curves of the pristine sample of $\text{Co}_9\text{S}_8@\text{N-S-HPC}$ and the sample after 5000 cycles, (d) LSV curves of samples for the HER at 5 mV s^{-1} and a rotating speed of 2000 rpm, (e) Tafel plots of samples, (f) LSV curves of the pristine sample of $\text{Co}_9\text{S}_8@\text{N-S-HPC}$ and the sample after 1000 cycles.

pathway [51]. The amount of hydrogen gas evolved in the electrolysis cell was also measured with the Faraday efficiencies greater than 97% (Fig. S8). To evaluate the stability of the $\text{Co}_9\text{S}_8@\text{N-S-HPC}$ electrocatalyst, the test was evaluated by cycling the electrode potential between -0.3 and +0.2 V vs. RHE with a sweep rate of 100 mV s^{-1} for 1000 cycles (Fig. 4f). Clearly, $\text{Co}_9\text{S}_8@\text{N-S-HPC}$ shows negligible decline

for both the HER onset overpotential and the cathodic current density, indicating superior stability of the catalyst under the operating conditions. The excellent catalytic activity and stability demonstrate that $\text{Co}_9\text{S}_8@\text{N-S-HPC}$ could be a promising HER electrocatalyst.

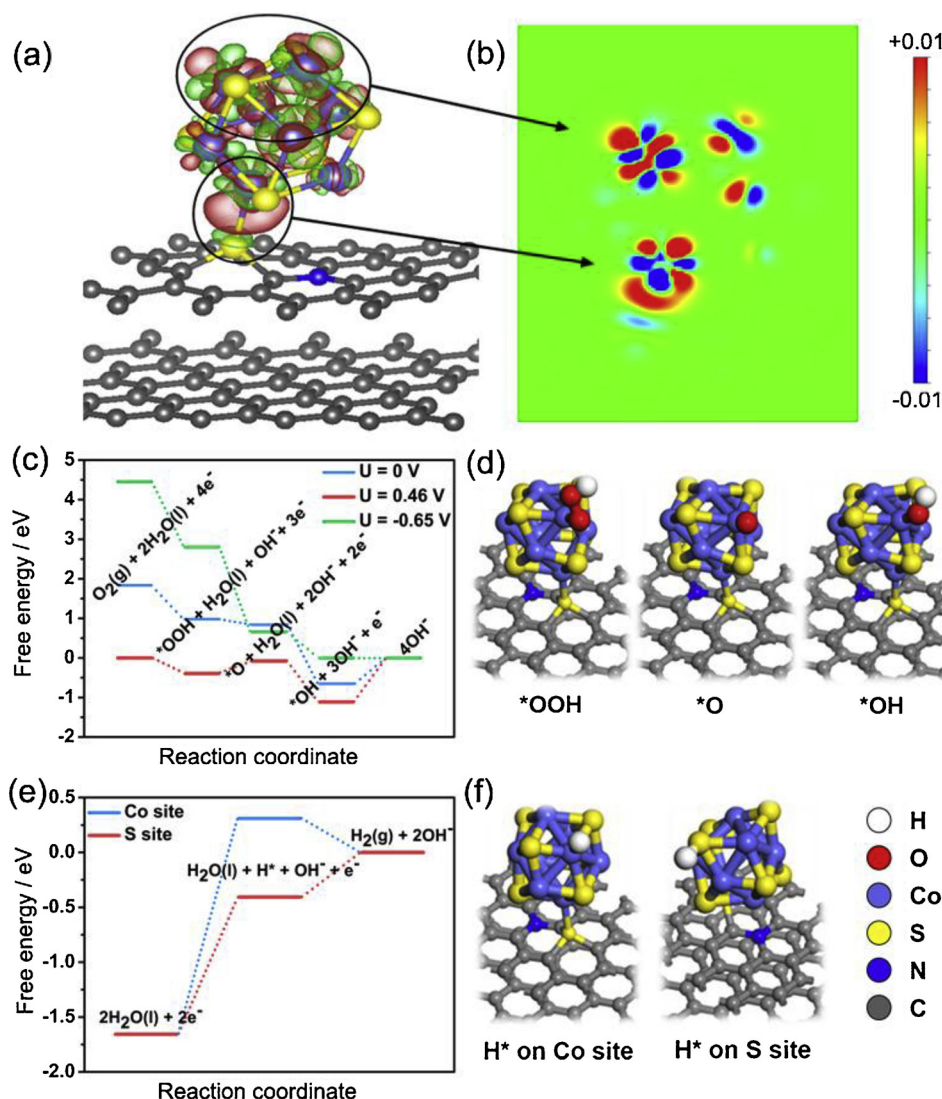


Fig. 5. (a) Isosurface of electron density difference for $\text{Co}_9\text{S}_8@\text{N-S-HPC}$ (isovalue = $\pm 0.003|e|/\text{bohr}^3$; the electron accumulation and depletion are represented by red and green surfaces, respectively), (b) 2D slice perpendicular to the N-S-HPC surface of electron density difference ($\Delta\rho$ is indicated according to the colorbar on the right; unit is $|e|/\text{bohr}^3$), (c) Free energy diagram for ORR over $\text{Co}_9\text{S}_8@\text{N-S-HPC}$ in alkaline media, (d) Structures of $^*\text{OOH}$, $^*\text{O}$, and $^*\text{OH}$ states, (e) Free energy diagram for HER over $\text{Co}_9\text{S}_8@\text{N-S-HPC}$ in alkaline media, (f) Structures of H^* on Co and S sites. (For interpretation of the references to colour in this figure legend, the reader is referred to the web version of this article).

3.3. DFT calculations

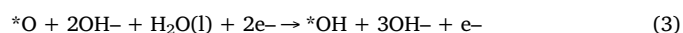
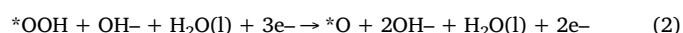
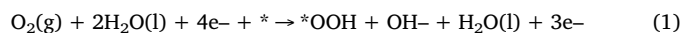
In order to obtain mechanistic insights into ORR and HER over $\text{Co}_9\text{S}_8@\text{N-S-HPC}$, we performed first-principles calculations based on density functional theory plus Hubbard U (DFT + U) with Grimme et al's D3 dispersion correction to study the structure of $\text{Co}_9\text{S}_8@\text{N-S-HPC}$ and the reaction mechanisms (see SI for computational details) [52,53]. We used generalized gradient approximation (GGA) parameterized by Perdew–Burke–Ernzerhof in the calculations [54]. Hubbard U correction was used to treat the strong on-site Coulomb interaction which was poorly described by GGA in the system. Free energy diagrams along reaction pathway were obtained using the scheme based on Nørskov et al.'s computational hydrogen electrode model [55]. We found Co_9S_8 particle can anchor in N-S-HPC via a Co-S bond with a bond length of 2.26 Å (Fig. S1). No covalent bond was formed between the Co and N. Moreover, there is no covalent bond found between Co_9S_8 particle and pure graphite substrate. The Co_9S_8 particle adsorbed on a graphite without doped S and N mainly via van der Waals interactions. It indicates that the presence of doped S atoms enhance the binding of Co_9S_8 particle and N-S-HPC, which may be the cause of the superior long-term stability of $\text{Co}_9\text{S}_8@\text{N-S-HPC}$ in working conditions.

To investigate the change of electronic structure of Co_9S_8 caused by the support (N-S-HPC), the electron density difference ($\Delta\rho$) was calculated using the following equation:

$$\Delta\rho = \rho(\text{Co}_9\text{S}_8@\text{N-S-HPC}) - \rho(\text{Co}_9\text{S}_8) - \rho(\text{N-S-HPC})$$

It can be seen from the isosurface and 2D slice view of the electron density difference (Fig. 5a and b) that both electron accumulation and depletion around the Co atoms are significant, indicating there is a strong electron transfer in d orbitals of Co atoms when Co_9S_8 supported on N-S-HPC. The electron transfer between N-S-HPC and Co_9S_8 is negligible. The sums of atomic charges for N-S-HPC and Co_9S_8 obtained by Bader charge analysis are only +0.046 $|e|$ and -0.046 $|e|$, respectively [56,57]. These suggest that N-S-HPC only transfers very little electrons to Co_9S_8 but affects the electronic structure of the supported Co_9S_8 strongly.

We considered the four-electron pathway for ORR in alkaline medium:

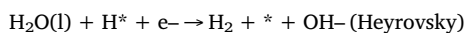
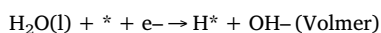


where the asterisk (*) indicates an active site or the chemisorbed state of the species.

We chose Co site as an active site to study the ORR pathway according to Sidik and Anderson's work [14]. Fig. 5c shows the free

energy diagram for four-electron ORR pathways. The structures of the intermediates are shown in Fig. 5d. The trends of the free energy profiles are consistent with Zhong et al.'s work [26]. The difference in the values of free energies is due to the different levels of theory (PBE + U -D3 versus PBE) and models. At $U = 0$, the overall reaction ($O_2(g) + 2H_2O(l) + 4e^- \rightarrow 4OH^-$) is exothermic by 1.84 eV in alkaline media (pH = 13). All reaction steps are downhill except for the last step, implying the reduction of $*OH$ to OH^- is the potential determining step. $U = 0.46$ V (1.84 eV/4e) is the equilibrium potential. At the equilibrium potential, steps (2) and (4) are uphill in free energy, suggesting the active sites would be covered by $*OOH$ and $*OH$. The accumulation of these species would hinder the adsorption of O_2 on active sites. All steps become downhill when applying a negative voltage $U = -0.65$ V.

For HER in alkaline media, Volmer-Heyrovsky process was considered in the calculations according to the deduction based on the Tafel slope in our experiments:



where the asterisk (*) indicates an active site or the chemisorbed state of the species.

We considered the pathways activated by Co and S sites, respectively (Fig. 5e and f). Free energy diagram for HER in alkaline media (pH = 14) at $U = 0$ is shown in Fig. 5e. The overall reaction ($2H_2O(l) + 2e^- \rightarrow H_2 + 2OH^-$) is endothermic by 1.65 eV. The free energy required to form the intermediate state for S site is 0.72 eV lower than that for Co site. It indicates the S sites are more favorable active sites for HER in alkaline media.

4. Conclusions

In summary, the composite of $Co_9S_8@N$ -S-HPC is prepared by a novel *in situ* formation approach, in which ZIF-8 is a sacrificial template material and provides nitrogen source, cobalt thiourea provides the sulfur source and *in situ* formation of Co_9S_8 NPs during the heat treatment process, polymeric resorcinol-formaldehyde acts as a shell and structure stabilizer. Attributing to the hollow nanostructure with high surface area and pore volume, heteroatom-doped carbon and the synergistic interactions of Co_9S_8 and N-S-HPC, the as-synthesized $Co_9S_8@N$ -S-HPC shows comparable electrochemical oxygen reduction activity to commercial 20 wt% Pt/C and outstanding stability even after 5000 cycles. Simultaneously, it also exhibits an excellent HER activity with a low onset overpotential, a small Tafel slope and a long-term durability in alkaline medium. Combined experimental and theoretical investigation indicated that unique nanostructure and synergistic interactions between Co_9S_8 and N-S-HPC play a crucial role to improve the electrocatalytic performance. The present work may open up a new route into the development of highly active nonprecious electrocatalysts with special morphology, tuned chemical nature and electrocatalytic bifunctions for both ORR and HER.

Acknowledgements

This work was supported by the National Key R&D Program of China (2016YFA0202801) and the National Natural Science Foundation of China (21521091, 21390393, U1463202, 21471089, 21671117, 21871159, 21890383). We thank the computing resources provided by Shanghai University's computing centers (ZIQIANG and QMS), Shanghai Supercomputer Center, and the National Supercomputing Center in Shenzhen, P.R. China.

Appendix A. Supplementary data

Supplementary material related to this article can be found, in the online version, at doi:<https://doi.org/10.1016/j.apcatb.2019.04.096>.

References

- [1] A. Kulkarni, S. Siahrostami, A. Patel, J.K. Nørskov, Understanding catalytic activity trends in the oxygen reduction reaction, *Chem. Rev.* 118 (2018) 2302–2312, <https://doi.org/10.1021/acs.chemrev.7b00488>.
- [2] M. Shao, Q. Chang, J.-P. Dodelet, R. Chenitz, Recent advances in electrocatalysts for oxygen reduction reaction, *Chem. Rev.* 116 (2016) 3594–3657, <https://doi.org/10.1021/acs.chemrev.5b00462>.
- [3] S. Dey, B. Mondal, S. Chatterjee, A. Rana, S. Amanullah, A. Dey, Molecular electrocatalysts for the oxygen reduction reaction, *Nat. Rev. Chem.* 1 (2017) 98, <https://doi.org/10.1038/s41570-017-0098>.
- [4] Y. Zheng, Y. Jiao, A. Vasileff, S. Qiao, The hydrogen evolution reaction in alkaline solution: from theory, single crystal models, to practical electrocatalysts, *Angew. Chem. Int. Ed.* 57 (2018) 7568–7579, <https://doi.org/10.1002/anie.201710556>.
- [5] Z.W. Seh, J. Kibsgaard, C.F. Dickens, I. Chorkendorff, J.K. Nørskov, T.F. Jaramillo, Combining theory and experiment in electrocatalysis: Insights into materials design, *Science* 355 (2017) eaad4998, <https://doi.org/10.1126/science.aaad4998>.
- [6] S. Lu, Z. Zhuang, Electrocatalysts for hydrogen oxidation and evolution reactions, *Sci. China Mater.* 59 (2016) 217–238, <https://doi.org/10.1007/s40843-016-0127-9>.
- [7] S. Liu, H. Zhang, X. Mu, C. Chen, Surface reconstruction engineering of twinned Pd_2CoAg nanocrystals by atomic vacancy inducement for hydrogen evolution and oxygen reduction reactions, *Appl. Catal. B Environ.* 241 (2019) 424–429, <https://doi.org/10.1016/j.apcatb.2018.09.067>.
- [8] K. Qu, Y. Wang, A. Vasileff, Y. Jiao, H. Chen, Y. Zheng, Polydopamine-inspired nanomaterials for energy conversion and storage, *J. Mater. Chem. A* 6 (2018) 21827–21846, <https://doi.org/10.1039/C8TA05245J>.
- [9] T. Sun, L. Xu, D. Wang, Y. Li, Metal organic frameworks derived single atom catalysts for electrocatalytic energy conversion, *Nano Res.* (2019), <https://doi.org/10.1007/s12274-019-2345-4>.
- [10] T. Sun, S. Zhang, L. Xu, D. Wang, Y. Li, An efficient multifunctional hybrid electrocatalyst: Ni_2P nanoparticles on MOF-derived Co,N-doped porous carbon polyhedrons for oxygen reduction and water splitting, *Chem. Commun.* 54 (2018) 12101–12104, <https://doi.org/10.1039/C8CC06566G>.
- [11] G. Wu, K.L. More, C.M. Johnston, P. Zelenay, High-performance electrocatalysts for oxygen reduction derived from polyaniline, iron, and cobalt, *Science* 332 (2011) 443, <https://doi.org/10.1126/science.1200832>.
- [12] W. Chen, J. Pei, C. He, J. Wan, H. Ren, Y. Wang, J. Dong, K. Wu, W. Cheong, J. Mao, X. Zheng, W. Yan, Z. Zhuang, C. Chen, Q. Peng, D. Wang, Y. Li, Single tungsten atoms supported on MOF-derived N-doped carbon for robust electrochemical hydrogen evolution, *Adv. Mater.* 30 (2018) 1800396, <https://doi.org/10.1002/adma.201800396>.
- [13] L.M. Rivera Gavidia, G. García, D. Anaya, A. Querejeta, F. Alcaide, E. Pastor, Carbon-supported Pt-free catalysts with high specificity and activity toward the oxygen reduction reaction in acidic medium, *Appl. Catal. B Environ.* 184 (2016) 12–19, <https://doi.org/10.1016/j.apcatb.2015.11.021>.
- [14] R.A. Sidik, A.B. Anderson, Co_9S_8 as a catalyst for electroreduction of O_2 : quantum chemistry predictions, *J. Phys. Chem. B* 110 (2006) 936–941, <https://doi.org/10.1021/jp054487f>.
- [15] A. Zhu, P. Tan, L. Qiao, Y. Liu, Y. Ma, J. Pan, Sulphur and nitrogen dual-doped mesoporous carbon hybrid coupling with graphite coated cobalt and cobalt sulfide nanoparticles: rational synthesis and advanced multifunctional electrochemical properties, *J. Colloid Interface Sci.* 509 (2018) 254–264, <https://doi.org/10.1016/j.jcis.2017.09.012>.
- [16] S. Huang, Y. Meng, S. He, A. Goswami, Q. Wu, J. Li, S. Tong, T. Asefa, M. Wu, M., N-, O-, and S-tridoped carbon-encapsulated Co_9S_8 nanomaterials: efficient bifunctional electrocatalysts for overall water splitting, *Adv. Funct. Mater.* 27 (2017) 1606585, <https://doi.org/10.1002/adfm.201606585>.
- [17] Z. Wu, J. Wang, M. Song, G. Zhao, Y. Zhu, G. Fu, X. Liu, Boosting oxygen reduction catalysis with N-doped carbon coated Co_9S_8 microtubes, *ACS Appl. Mater. Interfaces* 10 (2018) 25415–25421, <https://doi.org/10.1021/acsami.8b07207>.
- [18] Q. Lv, W. Si, J. He, L. Sun, C. Zhang, N. Wang, Z. Yang, X. Li, X. Wang, W. Deng, Y. Long, C. Huang, Y. Li, Selectively nitrogen-doped carbon materials as superior metal-free catalysts for oxygen reduction, *Nat. Commun.* 9 (2018) 3376, <https://doi.org/10.1038/s41467-018-05878-y>.
- [19] L. Yang, X. Zeng, W. Wang, D. Cao, Recent progress in MOF-derived, heteroatom-doped porous carbons as highly efficient electrocatalysts for oxygen reduction reaction in fuel cells, *Adv. Funct. Mater.* 28 (2018) 1704537, <https://doi.org/10.1002/adfm.201704537>.
- [20] K. Qu, Y. Zheng, S. Dai, S. Qiao, Graphene oxide-polydopamine derived N, S-doped carbon nanosheets as superior bifunctional electrocatalysts for oxygen reduction and evolution, *Nano Energy* 19 (2016) 373–381, <https://doi.org/10.1016/j.nanoen.2015.11.027>.
- [21] K. Qu, Y. Zheng, X. Zhang, K. Davey, S. Dai, S. Qiao, Promotion of electrocatalytic hydrogen evolution reaction on nitrogen-doped carbon nanosheets with secondary heteroatoms, *ACS Nano* 11 (2017) 7293–7300, <https://doi.org/10.1021/acsnano.7b03290>.
- [22] H. Wang, W. Wang, Y. Xu, S. Dong, J. Xiao, F. Wang, H. Liu, B. Xia, Hollow nitrogen-doped carbon spheres with Fe_3O_4 nanoparticles encapsulated as a highly active oxygen-reduction catalyst, *ACS Appl. Mater. Interfaces* 9 (2017) 10610–10617, <https://doi.org/10.1021/acsami.6b15392>.
- [23] Y. Wang, A. Kong, X. Chen, Q. Lin, P. Feng, Efficient oxygen electroreduction: hierarchical porous Fe-N-doped hollow carbon nanoshells, *ACS Catal.* 5 (2015) 3887–3893, <https://doi.org/10.1021/acscatal.5b00530>.
- [24] J. Wang, L. Li, X. Chen, Y. Lu, W. Yang, X. Duan, A Co-N/C hollow-sphere

- electrocatalyst derived from a metanilic CoAl layered double hydroxide for the oxygen reduction reaction, and its active sites in various pH media, *Nano Res.* 10 (2017) 2508–2518, <https://doi.org/10.1007/s12274-017-1455-0>.
- [25] L. Yu, H. Hu, H. Wu, X. Lou, Complex hollow nanostructures: synthesis and energy-related applications, *Adv. Mater.* 29 (2017) 1604563, <https://doi.org/10.1002/adma.201604563>.
- [26] H. Zhong, K. Li, Q. Zhang, J. Wang, F. Meng, Z. Wu, J. Yan, X. Zhang, In situ anchoring of Co₉S₈ nanoparticles on N and S co-doped porous carbon tube as bifunctional oxygen electrocatalysts, *NPG Asia Mater.* 8 (2016) e308, <https://doi.org/10.1038/am.2016.132>.
- [27] S. Zhang, A. Han, Y. Zhai, J. Zhang, W.-C. Cheong, D. Wang, Y. Li, ZIF-derived porous carbon supported Pd nanoparticles within mesoporous silica shells: sintering- and leaching-resistant core-shell nanocatalysts, *Chem. Commun.* 53 (2017) 9490–9493, <https://doi.org/10.1039/C7CC04926A>.
- [28] F.A. Cotton, O.D. Faut, J.T. Mague, Molecular and electronic structures of some thiourea complexes of cobalt(II), *Inorg. Chem.* 3 (1964) 17–21, <https://doi.org/10.1021/ic50011a004>.
- [29] H. Yang, S.J. Bradley, A. Chan, G.I. Waterhouse, T. Nann, P.E. Kruger, S.G. Telfer, Catalytically active bimetallic nanoparticles supported on porous carbon capsules derived from metal–organic framework composites, *J. Am. Chem. Soc.* 138 (2016) 11872–11881, <https://doi.org/10.1021/jacs.6b06736>.
- [30] L. Feng, G. Li, Y. Liu, Y. Wu, H. Chen, Y. Wang, Y. Zou, D. Wang, X. Zou, Carbon-armed Co₉S₈ nanoparticles as all-pH efficient and durable H₂-evolving electrocatalysts, *ACS Appl. Mater. Inter.* 7 (2015) 980–988, <https://doi.org/10.1021/am507811a>.
- [31] Y. Chen, S. Ji, Y. Wang, J. Dong, W. Chen, Z. Li, R. Shen, L. Zheng, Z. Zhuang, D. Wang, Y. Li, Isolated single iron atoms anchored on N-doped porous carbon as an efficient electrocatalyst for the oxygen reduction reaction, *Angew. Chem. Int. Ed.* 56 (2017) 6937–6941, <https://doi.org/10.1002/anie.201702473>.
- [32] J. Long, Y. Gong, J. Lin, Metal–organic framework–derived Co₉S₈@CoS@CoO@C nanoparticles as efficient electro- and photo-catalysts for the oxygen evolution reaction, *J. Mater. Chem. A* 5 (2017) 10495–10509, <https://doi.org/10.1039/C7TA01447C>.
- [33] X. Ma, X. Dai, X. He, Co₉S₈-Modified N, S, and P ternary-doped 3D graphene aerogels as a high-performance electrocatalyst for both the oxygen reduction reaction and oxygen evolution reaction, *ACS Sustain. Chem. Eng.* 5 (2017) 9848–9857, <https://doi.org/10.1021/acssuschemeng.7b01820>.
- [34] Q. Zhu, W. Xia, T. Akita, R. Zou, Q. Xu, Metal-organic framework-derived honeycomb-like open porous nanostructures as precious-metal-free catalysts for highly efficient oxygen electroreduction, *Adv. Mater.* 28 (2016) 6391–6398, <https://doi.org/10.1002/adma.201600979>.
- [35] H. Wang, C. Tang, Q. Zhang, A review of precious-metal-free bifunctional oxygen electrocatalysts: rational design and applications in Zn–air batteries, *Adv. Funct. Mater.* 28 (2018) 1803329, <https://doi.org/10.1002/adfm.201803329>.
- [36] J. Liu, C. Wu, D. Xiao, P. Kopold, L. Gu, P.A. van Aken, J. Maier, Y. Yu, MOF-derived hollow Co₉S₈ nanoparticles embedded in graphitic carbon nanocages with superior Li-ion storage, *Small* 12 (2016) 2354–2364, <https://doi.org/10.1002/smll.201503821>.
- [37] P. Ganesan, M. Prabu, J. Sanetuntikul, S. Shanmugam, Cobalt sulfide nanoparticles grown on nitrogen and sulfur codoped graphene oxide: an efficient electrocatalyst for oxygen reduction and evolution reactions, *ACS Catal.* 5 (2015) 3625–3637, <https://doi.org/10.1021/acscatal.5b00154>.
- [38] S. Zhang, D. Li, S. Chen, X. Yang, X. Zhao, S. Komarneni, D. Yang, Highly stable supercapacitors with MOF-derived Co₉S₈/carbon electrodes for high rate electrochemical energy storage, *J. Mater. Chem. A* 5 (2017) 12453–12461, <https://doi.org/10.1039/C7TA03070C>.
- [39] H. Li, X. Qian, C. Xu, S. Huang, C. Zhu, X. Jiang, L. Shao, L. Hou, Hierarchical porous Co₉S₈/nitrogen-doped carbon@MoS₂ polyhedrons as pH universal electrocatalysts for highly efficient hydrogen evolution reaction, *ACS Appl. Mater. Interfaces* 9 (2017) 28394–28405, <https://doi.org/10.1021/acsami.7b06384>.
- [40] A. Pendashteh, J. Palma, M. Anderson, R. Marcilla, NiCoMnO₄ nanoparticles on N-doped graphene: highly efficient bifunctional electrocatalyst for oxygen reduction/evolution reactions, *Appl. Catal. B Environ.* 201 (2017) 241–252, <https://doi.org/10.1016/j.apcatb.2016.08.044>.
- [41] D. Xiong, Q. Zhang, S.M. Thalluri, J. Xu, W. Li, X. Fu, L. Liu, One-step fabrication of monolithic electrodes comprising Co₉S₈ particles supported on cobalt foam for efficient and durable oxygen evolution reaction, *Chem.: A Eur. J.* 23 (2017) 8749–8755, <https://doi.org/10.1002/chem.201701391>.
- [42] M. Al-Mamun, Y. Wang, P. Liu, Y.L. Zhong, H. Yin, X. Su, H. Zhang, H. Yang, D. Wang, Z. Tang, H. Zhao, One-step solid phase synthesis of a highly efficient and robust cobalt pentlandite electrocatalyst for the oxygen evolution reaction, *J. Mater. Chem. A* 4 (2016) 18314–18321, <https://doi.org/10.1039/C6TA07962H>.
- [43] H. Zhu, J. Zhang, R. Yanzhang, M. Du, Q. Wang, G. Gao, J. Wu, G. Wu, M. Zhang, B. Liu, J. Yao, X. Zhang, When cubic cobalt sulfide meets layered molybdenum disulfide: a core–shell system toward synergetic electrocatalytic water splitting, *Adv. Mater.* 27 (2015) 4752–4759, <https://doi.org/10.1002/adma.201501969>.
- [44] A. Han, W. Chen, S. Zhang, M. Zhang, Y. Han, J. Zhang, S. Ji, L. Zheng, Y. Wang, L. Gu, C. Chen, Q. Peng, D. Wang, Y. Li, A polymer encapsulation strategy to synthesize porous nitrogen-doped carbon-nanosphere-supported metal isolated-single-atomic-site catalysts, *Adv. Mater.* 30 (2018) 1706508, <https://doi.org/10.1002/adma.201706508>.
- [45] M. Jahan, Q. Bao, K.P. Loh, Electrocatalytically active graphene–porphyrin MOF composite for oxygen reduction reaction, *J. Am. Chem. Soc.* 134 (2012) 6707–6713, <https://doi.org/10.1021/ja211433h>.
- [46] T. Sun, L. Xu, S. Li, W. Chai, Y. Huang, Y. Yan, J. Chen, Cobalt-nitrogen-doped ordered macro-/mesoporous carbon for highly efficient oxygen reduction reaction, *Appl. Catal. B Environ.* 193 (2016) 1–8, <https://doi.org/10.1016/j.apcatb.2016.04.006>.
- [47] L. Zhang, X. Wang, R. Wang, M. Hong, Structural evolution from metal–organic framework to hybrids of nitrogen-doped porous carbon and carbon nanotubes for enhanced oxygen reduction activity, *Chem. Mater.* 27 (2015) 7610–7618, <https://doi.org/10.1021/acs.chemmater.5b02708>.
- [48] X. Xiao, D. Huang, Y. Fu, M. Wen, X. Jiang, X. Lv, M. Li, L. Gao, S. Liu, M. Wang, C. Zhao, Y. Shen, Engineering NiS/Ni₂P heterostructures for efficient electrocatalytic water splitting, *ACS Appl. Mater. Inter.* 10 (2018) 4689–4696, <https://doi.org/10.1021/acsami.7b16430>.
- [49] X. Xu, F. Nosheen, X. Wang, Ni-decorated molybdenum carbide hollow structure derived from carbon-coated metal–organic framework for electrocatalytic hydrogen evolution reaction, *Chem. Mater.* 28 (2016) 6313–6320, <https://doi.org/10.1021/acs.chemmater.6b02586>.
- [50] B. Huang, Y. Liu, Z. Xie, Biomass derived 2D carbons via a hydrothermal carbonization method as efficient bifunctional ORR/HER electrocatalysts, *J. Mater. Chem. A* 5 (2017) 23481–23488, <https://doi.org/10.1039/C7TA08052B>.
- [51] X. Yu, J. Zhao, L. Zheng, Y. Tong, M. Zhang, G. Xu, C. Li, J. Ma, G. Shi, Hydrogen evolution reaction in alkaline media: alpha- or beta-nickel hydroxide on the surface of platinum? *ACS Energy Lett.* 3 (2018) 237–244, <https://doi.org/10.1021/acscenergylett.7b01103>.
- [52] S.L. Dudarev, G.A. Botton, S.Y. Savrasov, C.J. Humphreys, A.P. Sutton, Electron-energy-loss spectra and the structural stability of nickel oxide: an LSDA+U study, *Phys. Rev. B* 57 (1998) 1505–1509, <https://doi.org/10.1103/PhysRevB.57.1505>.
- [53] S. Grimme, J. Antony, S. Ehrlich, H. Krieg, A consistent and accurate *ab initio* parametrization of density functional dispersion correction (DFT-D) for the 94 elements H–Pu, *J. Chem. Phys.* 132 (2010) 154104, <https://doi.org/10.1063/1.3382344>.
- [54] J.P. Perdew, K. Burke, M. Ernzerhof, Generalized gradient approximation made simple, *Phys. Rev. Lett.* 77 (1996) 3865–3868, <https://doi.org/10.1103/PhysRevLett.77.3865>.
- [55] J.K. Nørskov, J. Rossmeisl, A. Logadottir, L. Lindqvist, J.R. Kitchin, T. Bligaard, H. Jónsson, Origin of the overpotential for oxygen reduction at a fuel-cell cathode, *J. Phys. Chem. B* 108 (2004) 17886–17892, <https://doi.org/10.1021/jp047349j>.
- [56] R.F.W. Bader, *Atoms in Molecules: A Quantum Theory*, Oxford University Press, New York, USA, 1990.
- [57] W. Tang, E. Sanville, G. Henkelman, A grid-based bader analysis algorithm without lattice bias, *J. Phys. Condens. Matter* 21 (2009) 084204, <https://doi.org/10.1088/0953-8984/21/8/084204>.